Journal of Environmental Management 370 (2024) 122996

Contents lists available at ScienceDirect

Journal of Environmental Management

journal homepage: www.elsevier.com/locate/jenvman

Research article

Ternary g-C_3N_4/Co_3O_4/CeO_2 nanostructured composites for electrochemical energy storage supercapacitors

Mule Vijayalakshmi [a], Rui Wang [a], Won Young Jang [a], Raghava Reddy Kakarla [b], Ch Venkata Reddy [a,**], Fernando Alonso-Marroquin [c], P.M. Anjana [d], Bai Cheolho [a,***], Jaesool Shim [a,****], Tejraj M. Aminabhavi [d,e,*]

[a] School of Mechanical Engineering, Yeungnam University, 280 Daehak-ro, Gyoungsan-si, Gyeongsangbuk-do, 38541, Republic of Korea
[b] School of Chemical and Biomolecular Engineering, The University of Sydney, Sydney, NSW, 2006, Australia
[c] Centre of Integrative Petroleum Research, King Fahd University of Petroleum and Minerals, Dhahran, 31261, Saudi Arabia
[d] Center for Energy and Environment, School of Advanced Sciences, KLE Technological University, Hubballi, 580 031, Karnataka, India
[e] Korea University, Seoul, 02841, Republic of Korea

ARTICLE INFO

Handling editor: Raf Dewil

Keywords:
Co_3O_4 flowers
CeO_2
Carbon materials
Ternary heterostructures
Electrochemical properties
Supercapacitors

ABSTRACT

Extensive use of fossil fuels causes heavy discharge of carbon dioxide, depleting energy resources and this requires environmentally friendly and effective energy storage materials. Hybrid supercapacitors (HSCs) are recently developed as effective energy storage materials enabling high capacitance retention rate and quick charging. Herein, synthesis of two-dimensional g-C_3N_4 nanosheets supported onto three-dimensional flower-like Co_3O_4/CeO_2 (CoCe) ternary synergistic heterostructures are developed as effective electrodes for hybrid supercapacitor applications. Addition of g-C_3N_4 produces substantial surface active sites, enabling its synergistic effect with CoCe to enhance electrochemical performance having exceptional conductivity. The CoCe/g-C_3N_4 ternary composite electrode exhibits a higher specific capacitance of 1088.3 F g^{-1} at 1 A g^{-1} with 96 % of recycling stability over 5000 cycles, which is ~5.5 and ~5 folds higher specific capacitance than the pristine g-C_3N_4 and CoCe electrodes. EIS analysis revealed that CoCe/g-C_3N_4 electrode offered reduced charge transfer resistance compared to pristine electrodes. The fabricated two-electrode HSC device displays outstanding retention after 10,000 cycles with an ultra-high specific capacitance of 119.8 F g^{-1}, excellent energy density 37.4 Wh kg^{-1} and power density of 749.9 W kg^{-1}. This research showcases the perspectives of CoCe/g-C_3N_4 ternary electrodes in hybrid supercapacitors and other renewable energy storage devices.

1. Introduction

In recent years, efforts are devoted towards clean and renewable energy sources due to fast increase in ecological contamination as a result of high usage of fossil fuels (Bhatt et al., 2024), (Reddy et al., 2022). Developing effective energy storage devices is therefore crucial to address energy calamity and growing demands of energy storage systems (Kundu et al., 2023), (Jang et al., 2023). Among the renewable energy storage devices, hybrid supercapacitors (HSCs) are the acceptable energy storage systems owing to their rapid charge/discharge cycle efficiency, higher power density, outstanding cyclic stability, eco-friendly and prospective practicality (Reddy et al., 2021), (Tuna et al., 2024). Nevertheless, HSCs have characteristically lesser energy density than batteries, which limits their practical applications (Chau et al., 2024), (Young Jang et al., 2023). It is, therefore, necessary to further enhance HSCs energy density, power density and wider voltage window (Zhang et al., 2022). It is thus necessary to explore innovative electrodes to enhance the capacity and energy density (Wang et al., 2023a).

Lately, heterostructured ternary electrode systems are being developed owing to their large surface area to generate high reaction sites. Heterostructured electrode surface area and morphology can influence

* Corresponding authors.
** Corresponding author.
*** Corresponding authors.
**** Corresponding author.
E-mail addresses: cvrphy@gmail.com (C.V. Reddy), chbai@yu.ac.kr (B. Cheolho), jshim@ynu.ac.kr (J. Shim), aminabhavit@gmail.com (T.M. Aminabhavi).

https://doi.org/10.1016/j.jenvman.2024.122996
Received 10 August 2024; Received in revised form 15 October 2024; Accepted 20 October 2024
Available online 24 October 2024

the electrochemical properties of HSCs, thus enhancing specific capacitance (Zhang et al., 2023), (Sethi et al., 2020). Hence, the preparation of ternary heterostructured composites with high specific surface area is needed. In recent years, transition metal oxides (MoO_3, CoO, NiO, and Co_3O_3, etc.) have been used as electrode materials in renewable energy storage devices owing to their outstanding electro-activity, inexpensive with natural abundance and having good electrical properties as well as high theoretical capacitance (Gao et al., 2015).

Among the various systems, spinal Co_3O_4 has received great attention due to its ease of availability, ample storage, and ecological advantages as well as its diverse valences (Co^{2+} and Co^{3+}) of Co cations (Li et al., 2015), (Lv et al., 2015). However, Co_3O_4 capacitance is still lower than its theoretical capacitance (~3000 F g^{-1}) due to its deprived conductivity and slow contribution of Faradaic nature, which restricts its rate of charge/discharge ability and recycling retaining activity (Li et al., 2018). In order to overcome these issues, an effective method is to upsurge cobalt oxide conductivity by introducing a suitable lower electronegativity material to improve the hybrid composites (Zhang et al., 2017a). Among these, rare earth CeO_2 with distinctive 4f5d electronic configuration has been considered useful owing to its exceptional properties such as higher oxygen storing ability, tunable vacancies and redox properties (Qi et al., 2014), (Huang et al., 2021a). After the introduction of CeO_2, exchange of valence state between Ce^{3+} and Ce^{4+} can fasten the electron transmission to increase electroactivity of the electrodes (Bhatt et al., 2024), (Xia et al., 2020).

Heterojunctions can attain fast electroactivity of the electrodes, and hence, they are suitable for boosting electrochemical activity using heterojunctions (Lian et al., 2016). For instance, CoO@Co-Cu-S and $CoS/NiCo_2S_4$ heterostructures with enhanced capacitance and decent cycling constancy have been reported by Lu et al. (2019) and Zeng et al. (2015). Such improved specific capacitance might be due to electrical properties, improved charge transmission and interface electric field (Zheng et al., 2016). Additionally, interaction between the two materials would facilitate the movement of ions and electrons. Nevertheless, fabrication of electrodes from a single material cannot fulfill targeted goals of the device. In such a situation, efforts have been pursued to examine the hybrid heterostructured ternary composites with distinctive 3D-like structures having exceptional capacitance to develop superior electrochemical properties of the electrodes.

Carbon-based systems have amazing consequences such as ternary composites, which are ideal for use with other electrode materials (Shin et al., 2023). These materials have created greater interest in energy storage systems that can be remarkably energetic owing to their well-arranged permeable frameworks, excellent chemical stability with higher specific surface area and electrical conductivity (Tareen et al., 2022). Among such materials, g-C_3N_4 semiconductors have shown considerable interest in photocatalysis, energy conversion, and energy storage due to their exceptional activity in electrode construction, extended specific surface area, ease of fabrication and less expensive (Zhang et al., 2019), (Maruthasalamoorthy et al., 2023). Furthermore, using g-C_3N_4 with other materials will enhance electrochemical efficacy to improve the total energetic sites of the heterostructures such as in 2D g-C_3N_4, which has a suitable surface area. Likewise, g-C_3N_4 triazine ring has a robust covalent bond, which provides extraordinary thermal and chemical stability (Bai et al., 2022).

Inspired by the above findings, hydrothermal synthesis was used to prepare 2D g-C_3N_4 supported hierarchical 3D flower-like Co_3O_4/CeO_2 ternary heterostructured composite to investigate electrochemical performances of HSCs electrodes. These ternary composites are prepared to improve electrical conductivity and specific surface area by joining g-C_3N_4 nanosheets with CoCe hierarchical flowers. The g-C_3N_4 nanosheets are then added to improve CoCe electrochemical performance due to its exceptional features. The prepared ternary heterostructured composites are investigated for microstructural, optical, and electrochemical properties. Their electrochemical performances are characterized using three electrode system in 2M KOH electrolyte. Notably, the ternary heterostructured electrode attained ultra-high capacitance of 1088.3F g^{-1} at a current density of 1 A g^{-1}. Furthermore, a hybrid battery cell type fabricated supercapacitor (CoCe/g-C_3N_4//AC) showed extraordinary energy density of 37.4 Wh kg^{-1} and a power density of 749.9 W kg^{-1}. After 10,000 charge/discharge cycles, the capacity was retained up to 100% and the electrode system can be a suitable cathode material for renewable energy storage devices.

2. Experimental

2.1. Chemicals

Melamine ($C_3H_6N_6$), cerium (III) nitrate hexahydrate ($Ce(NO_3)_3{\cdot}6H_2O$), cobalt(II) nitrate hexahydrate ($Co(NO_3)_3{\cdot}6H_2O$), urea (H_2NCONH_2), de-ionized (DI) water, and ethanol, respectively were purchased from Sigma Aldrich (South Korea).

2.2. Preparation of g-C_3N_4, Co_3O_4/CeO_2 and Co_3O_4/CeO_2/g-C_3N_4 heterostructures

Thermal polymerization technique was used to prepare g-C_3N_4 powder in which 5 g of melamine powder was ground in an agate mortar for 45 min, placed in an alumina crucible and heated to 500 °C for 2h, resulting in g-C_3N_4 powder with a pale yellow color. A one-step hydrothermal preparation was used to synthesize hierarchical 3D flower-like cobalt oxide/cerium dioxide (Co_3O_4/CeO_2) heterostructured composites. Briefly, $Ce(NO_3)_3{\cdot}6H_2O$ (0.1 M) and Co $(NO_3)_3{\cdot}6H_2O$ (0.3 M) were liquefied in deionized water (100 mL) to which 1.1 g of urea were added under constant stirring for 1 h to which a suitable amount of g-C_3N_4 powder was added, then taken to Teflon-lined vessel and maintained at 120 °C for 10 h. After reaching room temperature, the centrifugation procedure was used to collect the attained sample and clean it with deionized water and ethanol. Then, it was heated to 500 °C for 2 h under N_2 atmosphere. The obtained Co_3O_4/CeO_2 composite material was labeled as CoCe, while the Co_3O_4/CeO_2/g-C_3N_4 ternary composite was designated as CoCe/g-C_3N_4.

2.3. Characterization of materials

PANalytical X'Pert PRO diffractometer (MPD for bulk powder, Diatome (United Kingdom)) was used to investigate crystal phase of the materials. Surface morphology and microstructures were investigated using S-4800 (SEM, Hitachi, LTD (Japan)) and Tecnai G2 F20 S-TWIN instruments (Netherland) (HRTEM). XPS (Thermo scientific instrument, UK) was used to examine the surface chemical composition, and the BET surface area of the samples was measured using BET theory and BJH desorption analysis (BET Physisorption Analyzer, Model 3-Flex, Micromeritics (USA)).

2.4. Electrochemical measurements

Three electrode potentiostat workstation (Bio-Logic Sp-200) was used to investigate electrochemical performance using the standard three-electrode instrument. The Pt wire, Hg/HgO, and the synthesized materials were used as a counter, reference and working electrodes in 2M KOH electrolyte solution. The battery-type coin-cell device was fabricated to examine the performance of the hybrid supercapacitor (HSCs) device.

2.5. Electrode preparation

For the preparation of working electrode, the synthesized samples, activated carbon black, and polyvinylidene fluoride (80:10:10) were uniformly mixed in N-methyl pyrrolidone solvent via ultrasonicaton for 30 min, which was coated onto Ni foam and desiccated at 120 °C for 12 h in a vacuum oven. The hybrid supercapacitor (HSC) assembly and

calculations are provided in the supplementary information (SI file).

3. Results and discussions

3.1. Structural analysis

X-ray diffraction was used to examine crystal structure of the synthesized g-C_3N_4, CoCe, and CoCe/g-C_3N_4 ternary heterostructures (see in Fig. 1). Pure CoCe sample (Fig. 1(a)) has strong peaks of cubic fluorite CeO_2 crystal phase with diffraction patterns observed at 28.5°, 33.0°, 47.4° and 56.3°, signifying (111), (200), (220), and (311) crystal planes; the distinctive peaks are assigned to JCPDS No: 34–0394 (Wang et al., 2021a), respectively. Similarly, peaks observed at 31.2°, 36.8°, 44.8°, 59.3° and 65.2° are ascribed to (220), (311), (400), (511) and (440) cubic spinal planes of Co_3O_4, the observed peaks are assigned to JCPDS No: 42–1467, respectively (Fig. 1(a)) (Yi et al., 2023). No impurity-related peaks were observed, indicating the purity of the prepared sample. Pure g-C_3N_3 (Fig. 1(b)) showed two diffraction peaks at 13.1°, 27.4° related to (100), (002) planes, which are ascribed to in-plane repetitive units and stacking of the conjugated aromatic structure, respectively (Du et al., 2023). With regard to CoCe/g-C_3N_4, the characteristic diffraction peaks of CoCe and g-C_3N_4 were identified, specifying co-existence of both the samples. The two new planes were identified at 19.0° (111) and 69.4° (400) in the ternary composite related to the planes of Co_3O_4 and CeO_2. These data specify that g-C_3N_4 sheets were effectively loaded onto the surface of CoCe without any changes in their crystal phases.

FESEM and TEM analysis were performed to observe the surface morphology and microstructures of the materials. Fig. 2 shows FESEM images of pure CoCe and CoCe/g-C_3N_4 samples, while Fig. 2(a–c) shows FESEM images of pure CoCe samples with different magnifications. As can be seen from the images, well-controlled 3D flower-like surface morphology was observed with the nanowires having lengths ranging from 1 to 10 μm. Similarly, Fig. 2(d–f) shows FESEM images of CoCe/g-C_3N_4 ternary hetero-structured composite with different magnifications, where g-C_3N_4 nanosheets are successfully attached to the surface of CoCe, but they did not modify the 3D CoCe surface morphology. The FESEM images showed successful synthesis of CoCe/g-C_3N_4 ternary hetero-structured composite. Likewise, TEM and HRTEM analysis were used to observe the microstructures of CoCe/g-C_3N_4 ternary composite as shown in Fig. 3. Fig. 3(a) shows TEM image of the ternary composite, demonstrating the combination of CoCe and g-C_3N_4 sheets. HRTEM image of the composite presented in Fig. 3(b) suggests that the identified lattice spacing at 0.46 nm and 0.27 nm are related to (111) and (200) planes of Co_3O_4 and CeO_2. Additionally, Co_3O_4 and CeO_2 diffraction rings can be identified in SAED image (Fig. 3(c)), which supports XRD and FESEM analysis.

3.2. Surface analysis

The N_2 adsorption/desorption was used to study surface analysis and pore structures of g-C_3N_4, CoCe, and CoCe/g-C_3N_4 ternary composites, respectively. Fig. 4(a) shows N_2 adsorption/desorption isotherms, where all the isotherms exhibited characteristic type IV adsorption–desorption curves that are distinctive with the H3 hysteresis loops, specifying the occurrence of the mesoporous structure. The evaluated surface area of g-C_3N_4, CoCe, and CoCe/g-C_3N_4 samples are 17.6, 34.5 and 51.2 m^2/g, signifying that the addition of g-C_3N_4 increased the specific surface area of the materials. Fig. 4(b) shows the average pore size distribution of the samples, where average pore sizes are ~20.8 nm, ~18.4 nm and ~16.7 nm for g-C_3N_4, CoCe, and CoCe/g-C_3N_4, respectively. Overall, CoCe/g-C_3N_4 ternary composite shows a larger specific surface area and smaller pore size than g-C_3N_4 and CoCe, which can offer more exposed active sites and plentiful open channels for the interphase mass transmission (Riyajuddin et al., 2021). The specific surface area and pore size of the ternary composite exhibit improved electrocatalytic performance compared to that of pristine samples.

XPS was used to study the elements and the corresponding chemical structures on the surface of the ternary composite sample; XPS data are displayed in Fig. 5. The survey XPS spectrum (Fig. 5 (a)) displayed the occurrence of Co, Ce, O, C, and N elements, respectively. The deconvoluted core level XPS spectra of Co 2p are illustrated in Fig. 5 (b). The peaks at 796.3 eV and 781.5 eV are ascribed to Co $2p_{1/2}$ and Co $2p_{3/2}$ of Co^{2+} state, while the other peaks identified at 794.4 eV and 779.6 eV are attributed to Co $2p_{1/2}$ and Co $2p_{3/2}$ of Co^{3+} state along with two peaks at 788.6 and 784.3 eV of Co^{2+} and Co^{3+}, respectively. This signifies that cobalt exists in the form of 3+ and 2+ (Zhong et al., 2020), (Wang et al., 2023b). The deconvoluted high resolution XPS spectra of Ce 3d spectra are presented in Fig. 5(c), from which eight separate peaks can be identified from Ce XPS spectra, disclosing two types of Ce states instantaneously existing as the distinctive peaks at 916.3, 907.2, 900.2, 897.9, 888.4 eV ($3d_{3/2}$), and 881.9 eV ($3d_{5/2}$) that are credited to Ce^{4+} state, while other peaks at 883.4 and 902.7 eV are related to Ce^{3+} $3d_{5/2}$ and $3d_{3/2}$ states, respectively; this is in consistence with he reported literature (Li et al., 2023), (Xiao et al., 2024); the results suggest that Ce^{4+} and Ce^{3+} coexist onto the surface of the sample. Moreover, Ce^{3+} species are from the reduction of Ce^{4+}, while Ce^{3+} was associated to oxygen vacancies development on CeO_x (Liu et al., 2019). The dissimilar valence states specify that the synthesized ternary composite has dissimilar types of cerium oxide, which confirms the formation of CeCo. The fitted O 1s spectra are presented in Fig. 5 (d), where two peaks are identified at 529.6 eV and 531.3 eV, which are credited to lattice oxygen

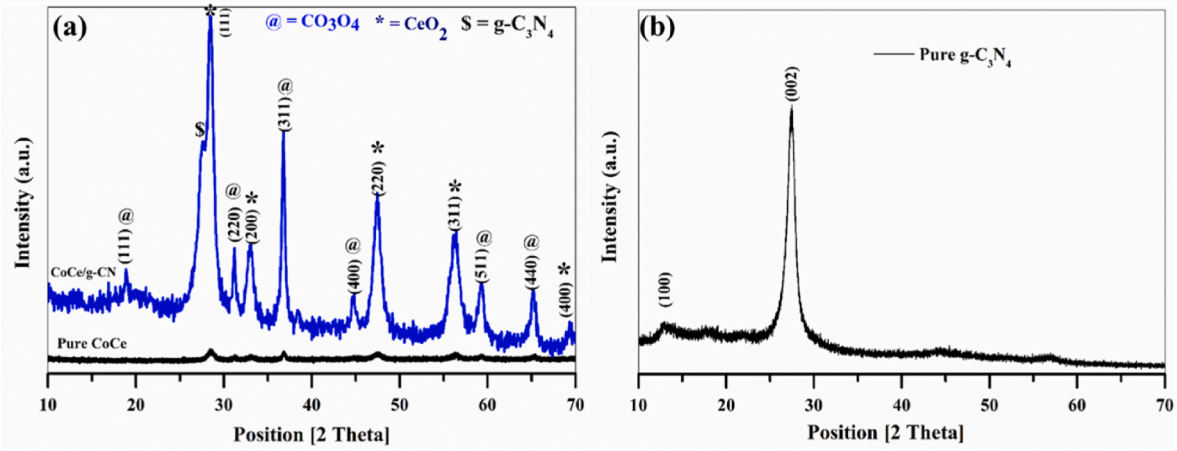

Fig. 1. XRD patterns of (a) Pure CoCe, CoCe/g-C_3N_4, and (b) pure g-C_3N_4 samples.

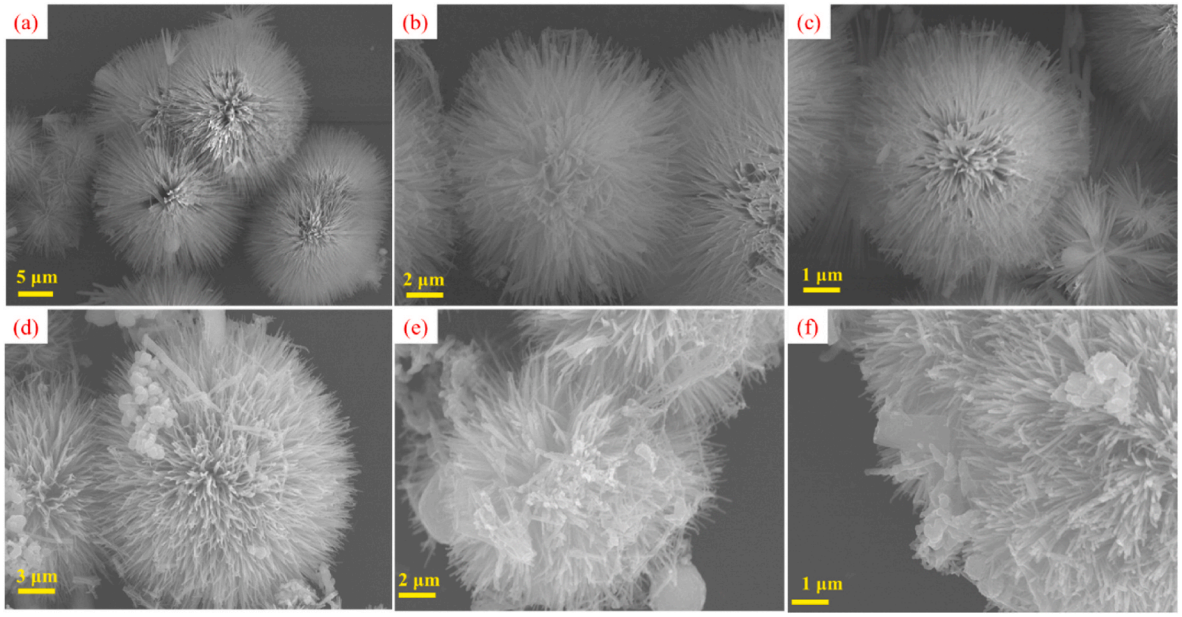

Fig. 2. FESEM images of (a–c) Pure CoCe, and (d–e) CoCe@g-C_3N_4 ternary composites sample.

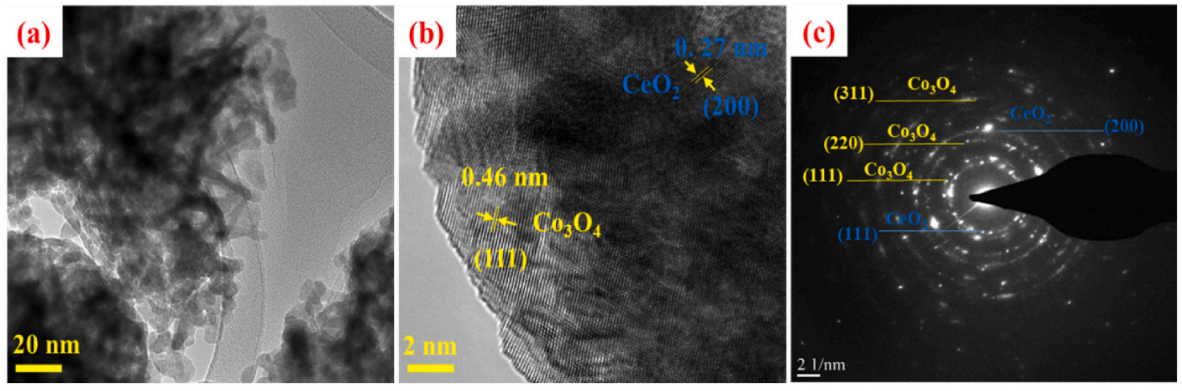

Fig. 3. (a) TEM, (b) HRTEM, and (c) SAED patterns of CoCe@g-C_3N_4 ternary composites sample.

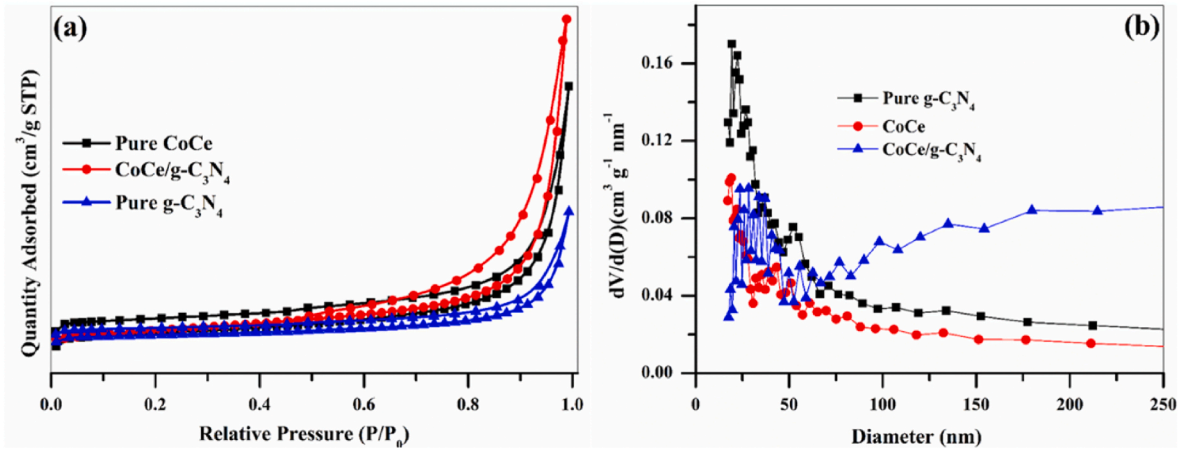

Fig. 4. (a) BET surface area analysis, (b) average pore size distribution of prepared samples.

in cobalt oxide and cerium oxide and metal-oxygen bonds (Huang et al., 2021b). Moreover, interactions between Co and Ce species may lead to the reduction of Ce^{4+} to Ce^{3+}. Hence, the development of oxygen vacancies is encouraged to sustain the charge impartiality, and these oxygen vacancies are necessary for the unfulfilled Lewis pair's creation (Zhang et al., 2017b), which could improve the performance of the subsequent electro-catalyst. Particularly, the peak at 529.6 eV suggests the presence of lattice oxygen initiated from the surface crystalline of

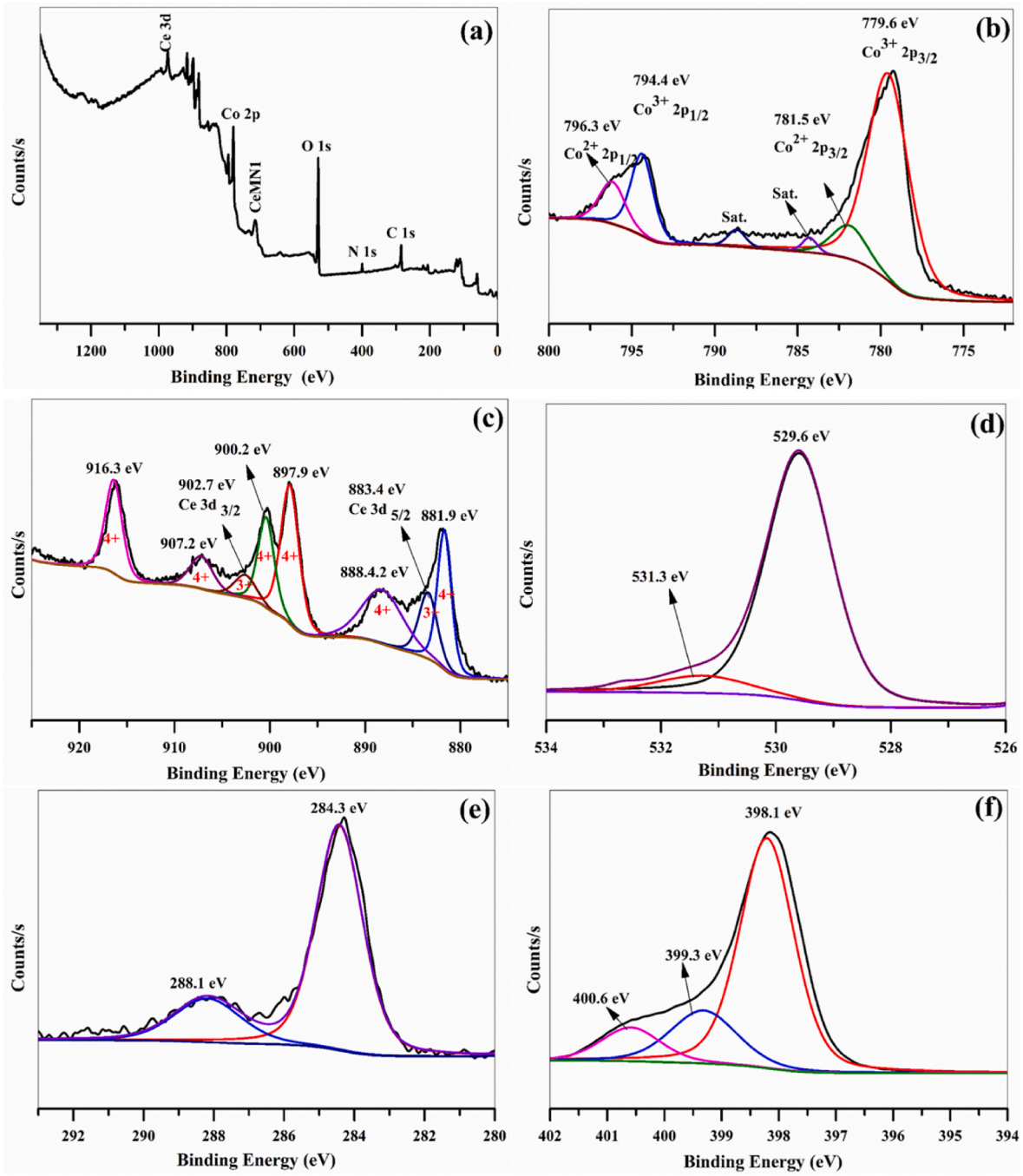

Fig. 5. XPS spectra (a) survey, (b) Co, (C) Ce, (d) O, (e) C, and (f) N of CoCe/g-C_3N_4 ternary composites sample.

cobalt oxide (Bao et al., 2015). Fig. 5 (e) illustrates C 1s XPS spectra, where two C–C/C=C, and C=O peaks are identified at 284.3 eV and 288.1 eV. The N1s XPS spectra are shown in Fig. 5 (f), where the peaks at 398.1, 399.3 and 400.6 eV are ascribed to pyridinic-N, pyrrolic-N, and quaternary-N, respectively (Wang et al., 2021b). XPS analysis confirmed the elemental chemical states in the ternary composite sample.

3.3. Electrochemical analysis

Electrochemical properties of the materials were investigated using three electrode system in 2M KOH electrolyte. Fig. 6(a) presents typical cyclic voltammetry (CV) curves for pristine CoCe, g-C_3N_4, and CoCe/g-C_3N_4 materials taken at the scanning rate of 30 mV s^{-1} in the working voltage window of 0–0.6 V. All the electrodes presented paired redox peaks, indicating that the energy storage involves fast and reversible redox reaction, a battery-type energy storage mode dominated by the intercalation or diffusion (Roy et al., 2024). Moreover, the redox peaks in the prepared electrodes are accredited to the multi-electron transmission reactions of $Co^{2+} \leftrightarrow Co^{3+} \leftrightarrow Co^{4+}$ and $Ce^{3+} \leftrightarrow Ce^{4+}$. At the same sweeping rate, redox peaks and curve areas of pure CoCe and g-C_3N_4 are smaller than those of CoCe/g-C_3N_4, indicating that heterogeneous CoCe/g-C_3N_4 electrode has a higher specific capacity and faster electrochemical reaction kinetic energy. The CoCe/g-C_3N_4 ternary electrode has a larger surface area, enormous active reaction sites and good electrical conductivity, which are beneficial to electrochemical performance, which is mostly attributed to superior electrical conductivity due to synergistic interaction between CoCe and g-C_3N_4 materials. Fig. 6(b) illustrates CV curves for CoCe/g-C_3N_4 ternary electrode at different scan

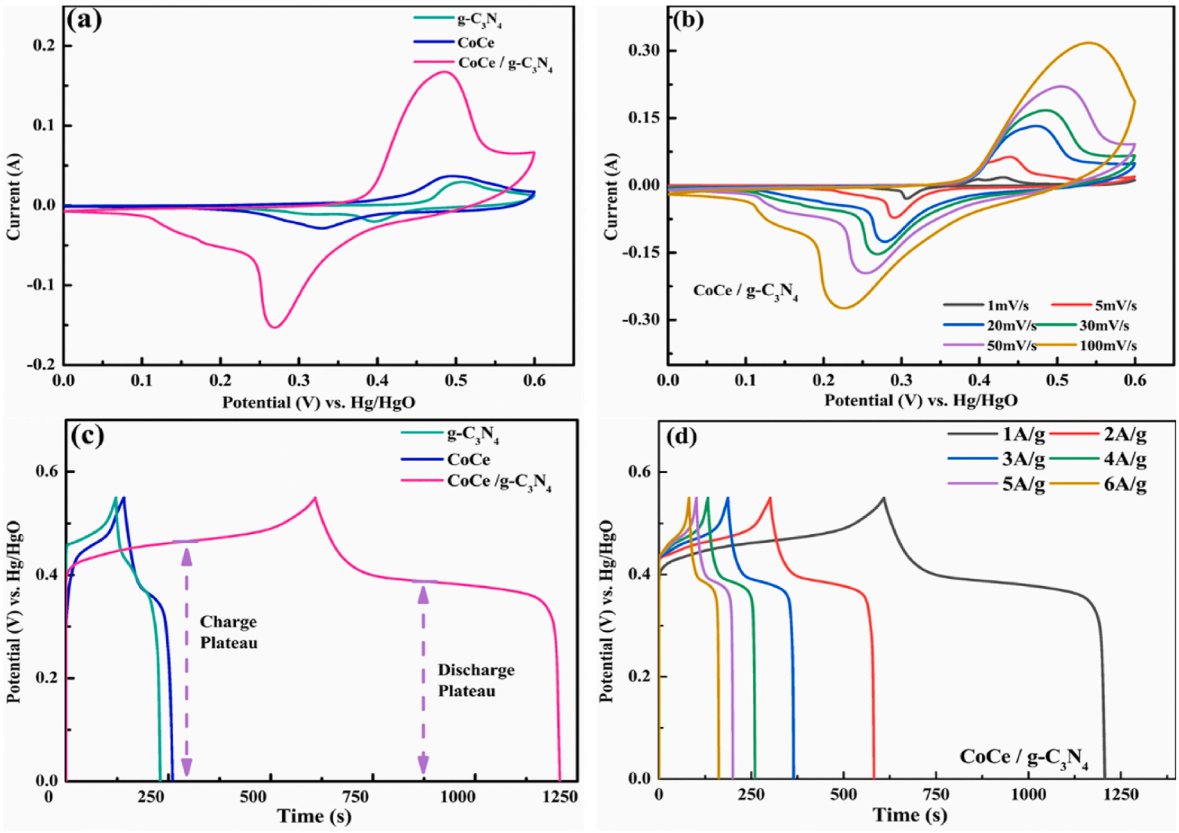

Fig. 6. a) The comparative CV profiles of prepared materials at 30 mV s^{-1}, b) The CV profiles of CoCe/g-C_3N_4 from 1 to 100 mV s^{-1}, c) The comparative GCD curves of materials at 1 A g^{-1}, d) The GCD curves of CoCe/g-C_3N_4 from 1 to 6 A g^{-1}.

rates. With increased scan rate, the consistency in shape indicates that the energy storage reaction of CoCe/g-C_3N_4 electrode is highly reversible and stable (pure CoCe, g-C_3N_4 electrodes; the CV curves at different rates are presented in Fig. S1 (a & b)). All the electrodes show specific current increases with the scan rates, signifying well rescindable Faradaic redox responses with an extensive potential separation for the quick galvanostatic charge/discharge procedure. Also, the redox peak position shifts to the corresponding potential with increasing the scan rate, representing electrodes as having excellent electrochemical reversibility (Liu et al., 2017).

Fig. 6 (c) displays galvanostatic charge/discharge (GCD) curves for g-C_3N_4, CoCe, and CoCe/g-C_3N_4 electrodes at 1 A g^{-1} current density. All the electrodes have a wide operating voltage window of 0–0.55 V. In contrast to conventional electric double layer capacitor (EDLC) and pseudo-capacitive electrodes, the GCD curve of hetero-structured electrode demonstrates distinct charging and discharging patterns, suggesting a non-linear relationship between voltage and charge storage/discharge within the specific range, attributed to additional capacitance phenomena associated with the electrode potential. Furthermore, these charge and discharge curves correspond to the prominently separated redox peaks in the CV curve, further proving that the storage mechanism of the electrode involves Faradaic redox reaction (Shao et al., 2018). As shown in Fig. 6(d), the GCD performance of CoCe/g-C_3N_4 at various current densities from 1 to 6 A g^{-1}. The GCD curves have shown consistently high symmetry under various current densities, suggesting their conventional reversibility in redox reactions, robust cycling, and rate capabilities. The GCD curves of pure g-C_3N_4, CoCe electrodes are illustrated in Fig. S1 (c & d) under similar conditions. The specific capacitance of g-C_3N_4, CoCe, and CoCe/g-C_3N_4 ternary hetero-structured electrodes as calculated from their respective GCD curves is presented in Fig. 7(a), where CoCe/g-C_3N_4 ternary electrode has ultra-high specific capacitance of 1088.3F g^{-1} at current density of 1 A g^{-1}, which is significantly higher than that of pure g-C_3N_4 (196.5 F g^{-1}) and CoCe (215.4 F g^{-1}) under similar conditions. In addition, CoCe/g-C_3N_4 ternary electrode displayed outstanding electrochemical performance (1088.3 Fg^{-1} at a current density of 1 A g^{-1}), which is higher than those reported on Co and Ce-based composites as shown in Table 1. In addition, CoCe/g-C_3N_4 ternary electrode shows excellent energy storage capacity at current densities of 2, 3, 4, 5, and 6 A g^{-1}, which are 1025.7, 973.7, 932.3, 896.1, and 872.3 F g^{-1}, respectively. These characteristics can be ascribed to two primary factors: (i) heterostructured material has a high surface area (SSA), which offers sufficient active sites, and provides efficient transport and diffusion channels for particle adsorption and desorption, contributing significantly to its superior electrochemical performance. (ii) The material benefits from the exceptional electrochemical reaction kinetics. (iii) Additionally, diffusion-dominated surface redox reactions produce stronger chemical energy compared to traditional ion adsorption and desorption compared to pristine electrodes.

The CoCe/g-C_3N_4 distinctive construction can efficiently avoid the accumulation of g-C_3N_4 sheets. Specifically, addition of g-C_3N_4 nanosheets to CoCe could offer a vast quantity of active sites and a large surface area. Additionally, the unique structure permits the formation of enormous interaction between the active material and the electrolyte, enabling the transfer of electrons/ions. Therefore, g-C_3N_4 nanosheets and CoCe may provide better mechanical strength and extended toughness. As illustrated in Fig. 7(b), the electrochemical impedance (EIS) curves reveal that CoCe/g-C_3N_4 electrode has the lowest contact resistance (R_s), charge transmission impedance (R_{ct}), and diffusion impedance (W_s) than the nascent electrodes, indicating its superior electrochemical performance (Rabbani et al., 2023) (Table S1 for specific results). This can be attributed to distinctive hetero-structure of CoCe/g-C_3N_4, which facilitates several beneficial factors. The CoCe/g-C_3N_4 ternary electrode exhibited lesser internal resistance (0.35

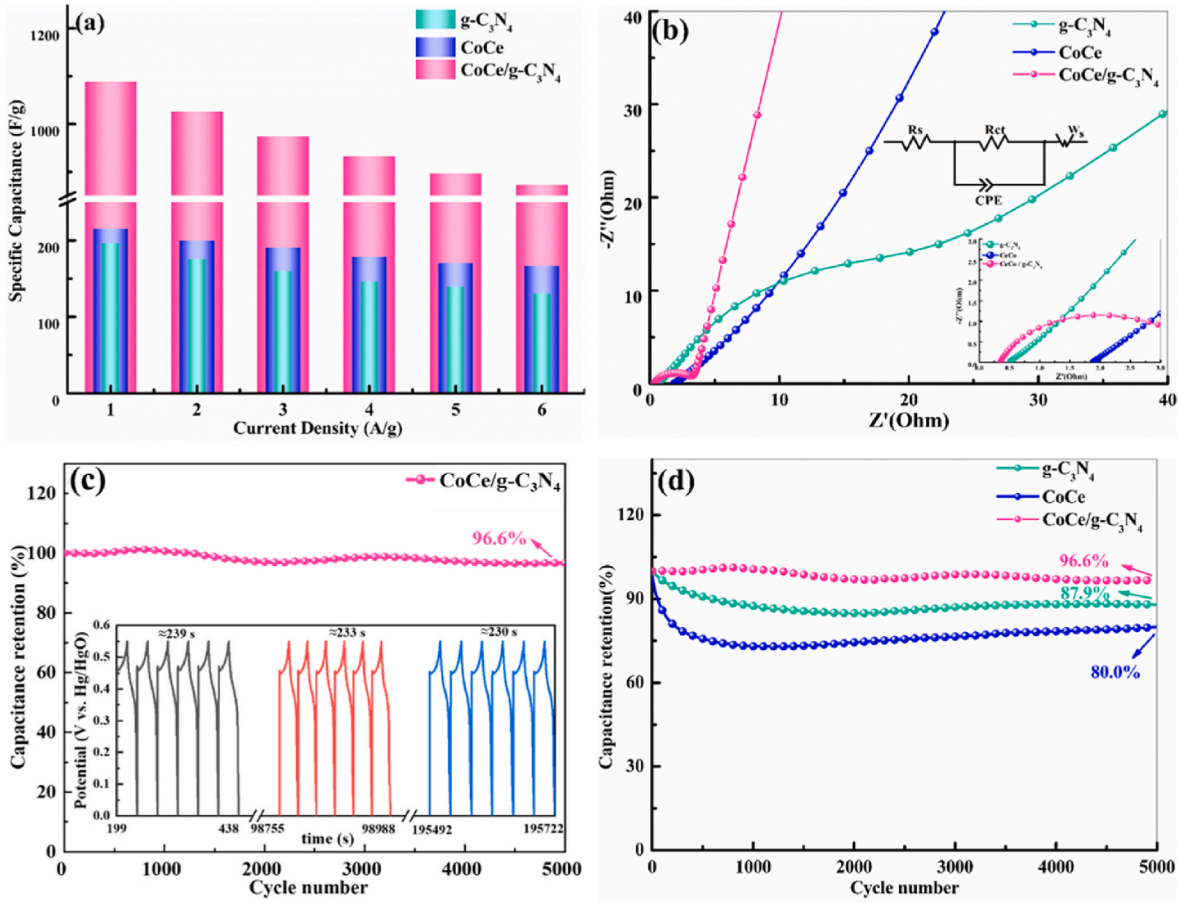

Fig. 7. (a) The specific capacitances of materials across a spectrum of current densities ranging from 1 to 6 A g^{-1}, (b) The Nyquist plots for materials with the specific equivalent circuit, (c) the cycling performance of CoCe/g-C_3N_4 during 5000 cycles with corresponding periodic GCD profiles, and (d) the comparison of capacitance retention for materials.

Ω), enlightening its higher conductivity. Also, CoCe/g-C_3N_4 ternary electrode shows a semicircle-like arc, signifying that lower charge transmission resistance (R_{ct}) occurs onto the surface electrode in interaction with the electrolyte. Also, from the EIS analysis, it is evident that CoCe/g-C_3N_4 electrode shows reduced charge transmission resistance onto the surface of the electrode, and hence, increased interfacial charge transmission, which offers abundant ion transport conductivity due to the addition of g-C_3N_4 sheets that has excellent conductivity (Ali et al., 2018). Thus, the combination of 3D flower-like CoCe with 2D g-C_3N_4 nanosheets could reduce the typical collapse issue observed in 2D materials (Kang et al., 2022), thereby enhancing the availability of the surface area for adsorption and desorption of the particles. This concurrently contributes to narrowing the energy band gap of the materials, thereby lowering the potential barrier for electron transport, thereby optimizing electrical conductivity to improve its electrochemical reaction dynamics (Fu et al., 2024). The CoCe/g-C_3N_4 electrode was tested up to 5000 cycles at a current density of 15A g^{-1}. The results presented in Fig. 7(c) demonstrate a capacitance retention rate of 96.6% after 5000 cycles. The GCD profile exhibits a remarkable consistency throughout the cycling process, with charging-discharging plateaus remaining intact, which underscores the materials' exceptional reversible cycling performance. Compared to pure g-C_3N_4 (87.9% capacity retention) and CoCe (80.0% capacity retention), ultra-high cyclic stability of CoCe/g-C_3N_4 stands out to be better in practical applications as shown in Fig. 7(d).

The study on electrode energy storage capabilities was also examined, mainly focusing on the energy storage reaction kinetics of CoCe/g-C_3N_4 ternary hetero-structured electrodes. Generally, the reversible mechanism of energy storage was understood to originate from two distinct electrochemical reaction mechanisms: the diffusion-controlled process (Faraday process) and the capacitance process (EDLC) (Yang et al., 2020). Throughout the CV cycle, the relationship between varying scanning rates (v) and resulting current (i) adheres to the following equations (Wang et al., 2007):

$$i = av^b \tag{1}$$

$$\log i = \log a + b \log v \tag{2}$$

where the value of b varies between 0.5 and 1. For b = 0.5; the behavior is controlled by diffusion, while for b = 1.0 it is controlled by the capacitance. The value b was evaluated from the slope of the logarithm of CV peak current I and scanning speed ν. The anode and cathode peak fitting results of the electrode are shown in Fig. 8(a), where at the apex of both the cathode and anode, the b values are 0.58 and 0.61, respectively, which fall in the range of 0.5–1.0, further substantiating a cooperative interplay between diffusion and capacitive control mechanisms that governs the entire energy storage operation. Furthermore, the parameter b approximates 0.5, which suggests that the energy storage mechanism of CoCe/g-C_3N_4 electrode closely resembles that of a battery, characterized predominantly by diffusion-controlled behavior. This implies higher energy density, similar to the principles governing battery operations, enhancing its ability for renewable energy storage devices. The quantitative distribution of diffusion and capacitance contribution were analyzed using the equation (Brezesinski et al., 2010):

$$i = k_1\nu + k_2\nu^{1/2} \tag{3}$$

Table 1
Comparison of electrochemical performance of relative-material electrodes.

Electrode Material	Specific Capacity	Electrolyte	Capacity Retention %	Cycle Number	Ref
CeCoSx-SA/GF	873 F g^{-1} (1 A g^{-1})	6 M KOH	87.1	5000	Reddy et al. (2021)
CdS/rGO/CeO_2	407 F g^{-1} (1 A g^{-1})	2 M KOH	96	5000	Ali et al. (2018)
Ce[Fe(CN)$_6$]	148 C/g (0.5 A g^{-1})	1 M KOH	74.5	5000	Xie et al. (2021)
Co-Fe LDHs	728 F g^{-1} (1 A g^{-1})	2 M	84	5000	Ma et al. (2016)
CeO_2@ZIF-8	131 F g^{-1} (1 A g^{-1})	3 M KOH	90	5000	Rabani et al. (2021)
Mn-Ni-Co Oxide	638 F g^{-1} (1 A g^{-1})	6 M KOH	96.3	6000	Li et al. (2014)
Ni-Co LDH/NiMoSx	404 mA h g^{-1} (3 mA cm^{-2})	3 M KOH	93.2	10,000	Kandula et al. (2019)
$Co(OH)_2$/$CoSe_2$//CNTs	1283.3 C/g (1 A g^{-1})	3 M KOH	96.3	4000	Song et al. (2021)
Co_3S_2/CoS/MoS_2	805.7 F g^{-1} (1A g^{-1})	3 M KOH	91.2	6000	Qiao et al. (2021)
Co_3O_4/Co$(OH)_2$	771.2 Fg^{-1} (1 A g^{-1})	5 M KOH	93.3	3000	Cho et al. (2020)
Co-Mo-O	302 F g^{-1} (1 A g^{-1})	1 M KOH	95.8	2000	Tian et al. (2017)
Co-MOF	578.6 F g^{-1} (1 A g^{-1})	1 M KOH	88.7	1000	Sun et al. (2020)
CoCe/g-C_3N_4	1088.3 Fg^{-1} (1 A g^{-1})	2 M KOH	100	5000	This work

where $k_1\nu$ is capacitive contribution current, and $k_1\nu^{1/2}$ is diffusion contribution current. Fig. 8 (b) shows the contribution distribution of the capacitance at 30 mV s^{-1} scan rate (distributions of capacitance contributions at various scanning rates, shown in Fig. S2. Fig. 8(c) summarizes the dispersal ratio of diffusion and capacitive contributions at different scan rates, suggesting that as the scanning rate increases, there is a progressive growth in the capacitance along with a simultaneous decrease in diffusion contribution. This phenomenon is ascribed to the nature of the Faraday reaction, which characterizes the battery-type energy storage through a slow and reversible redox process. At increased scanning rates, the temporal constraints imposed by semi-infinite diffusion reduce the reversible redox reaction time. Conversely, the occurrence of capacitive contribution (occurs immediately at both adjacent to the electrode surface) experienced a gradual increase. The comparative analysis of the two contributions reveals that ternary electrodes demonstrate superior electrochemical reaction kinetics. Specifically, diffusion contribution indicates enhanced energy density, a characteristic primarily associated with the battery performance. Conversely, the capacitive contribution reflects increased power density, which aligns more closely with the attributes of SCs. This differentiation underscores the potential of heterogeneous materials to optimize electrochemical properties for applications requiring high energy storage or rapid energy release. As a result, the ultra-high specific capacity and excellent recycle ability of the ternary electrode can be credited to the accessible electroactive surface area for faster reactions (Faradaic redox) and 3D hierarchical flower-like morphology self-possessed of the nanowire interfacial interaction, while the 2D g-C_3N_4 sheets enable quicker electrolyte ions and electrons transmission through the interrelating channels. These consequences specify the high practical usage of the ternary electrodes owing to their ultra-high specific capacitance, decent rate ability, and excellent cyclic constancy.

3.4. Hybrid supercapacitor device performance

The CoCe/g-C_3N_4 electrode demonstrates outstanding energy storage capabilities in addition to superior electrochemical reaction kinetics, providing a viable pathway for developing cathode electrodes of hybrid supercapacitors (HSCs). This configuration employed CoCe/g-C_3N_4 (two-electrode system) as the cathode material with 2M KOH electrolyte by utilizing commercially available activated carbon (AC) for the anode. The working voltage window of HSC was tested as shown in Fig. 9 (a). The results show that CoCe/g-C_3N_4//AC HSC works quite stable in the window of 0–1.6 V. At a higher applied voltage of more than 1.6 V, the cathode appears in an oxygen evolution reaction (OER) (Shao et al., 2018), which is not conducive to the cycle stability, which means that HSC has a broader working voltage window, indicating higher power density. Fig. 9 (b) depicts CV profiles of the device, recorded at varying scan rates. Integrating an AC anode into HSCs resulted in CV profile exhibiting the combined features of symmetrical redox peaks (battery-like behavior) and a rectangular-like shape (capacitive response), which is symbolic of HSC (Chatterjee and Nandi, 2021). Furthermore, the uniformity observed in CV profiles across various scan rates underscores HSCs enhanced stability and rate capability, highlighting their ability to improve the performance in energy storage applications with capacitive and battery-like attributes. A similar phenomenon was also observed in GCD curve of HSC (Fig. 9 (c)). A short charging and discharging platform and a symmetrical triangle line appeared, suggesting that HSC combines the dual characteristics of battery and supercapacitor.

The specific capacitance calculated from the GCD curves is depicted in Fig. 9 (d), where HSC demonstrated a noteworthy specific capacitance of 119.8 F g^{-1} at a current density of 1 A g^{-1}. Moreover, it maintained a commendable specific capacitance of 49.6 F g^{-1} even at the elevated current density of 20 A g^{-1}. The specific capacitance of CoCe/g-C_3N_4// AC HSC surpassed the recently reported data (Kim et al., 2023), (Ji et al., 2023), (Hadji et al., 2023), indicating that it maintains a strong performance under the conditions of high power demand. Energy and power densities are extensively recognized as vital device performance indicators for energy storage applications. According to GCD curve, the energy density and power density of HSC under different conditions

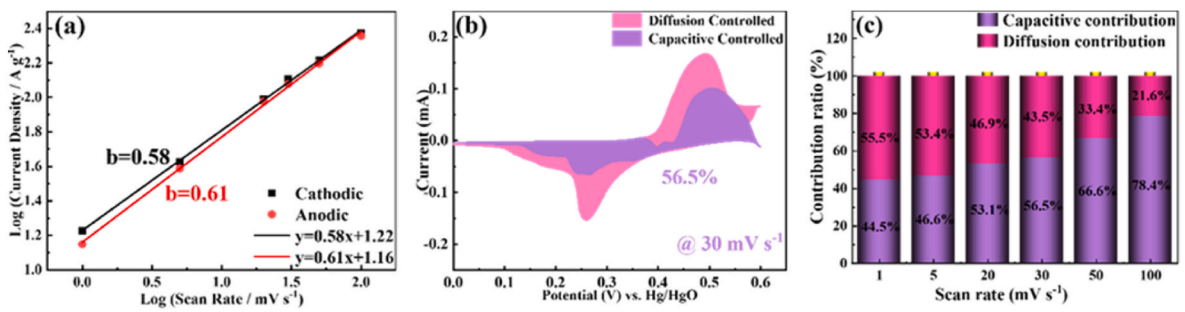

Fig. 8. (a) The b values of CoCe/g-C_3N_4 calculated from corresponding peak current and sweep rate, (b) The capacitive and diffusion contribution distributions of CoCe/g-C_3N_4 at 30 mV s^{-1}, and (c) The capacitive and diffusion fractions of CoCe/g-C_3N_4 at diverse scan rates.

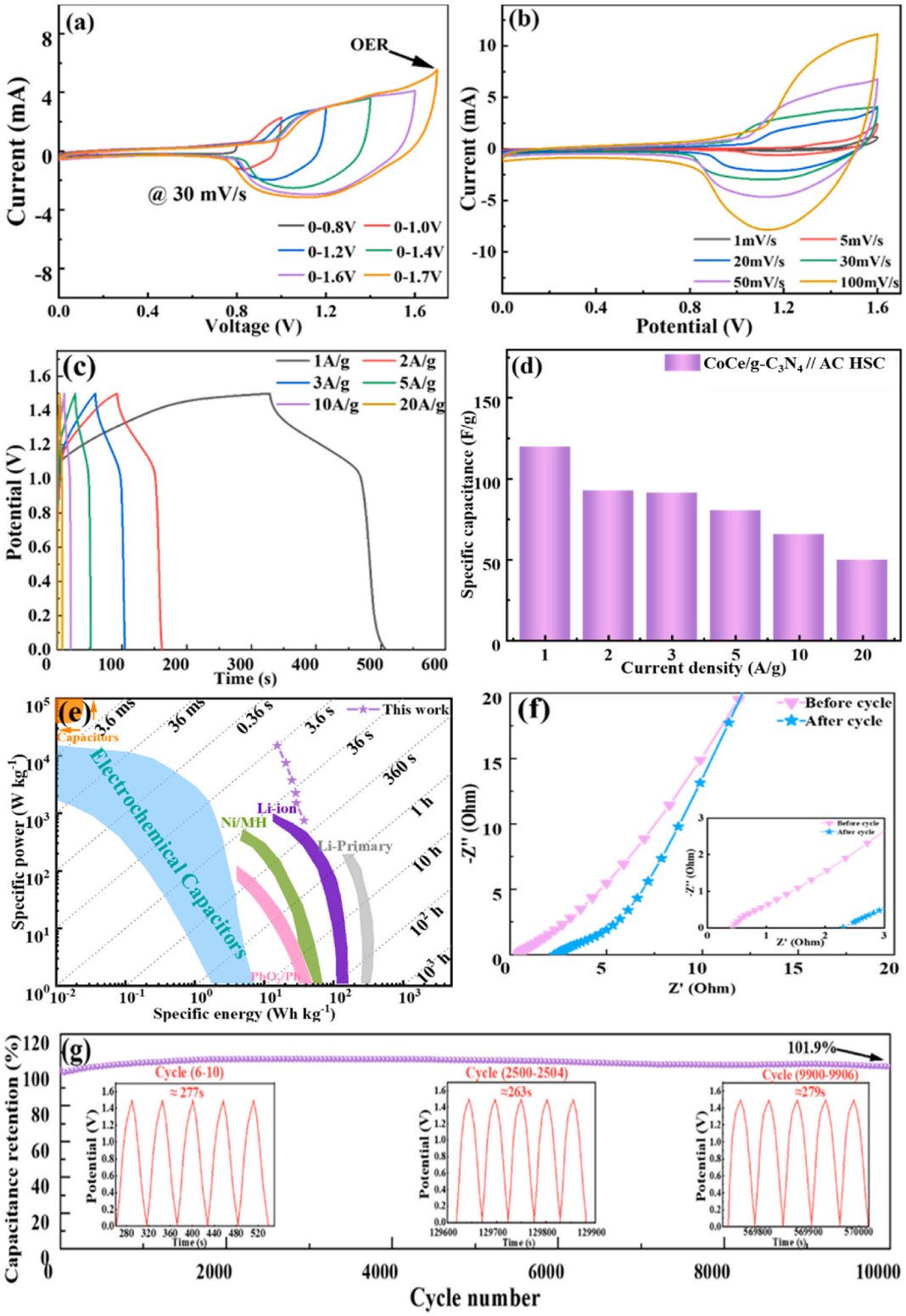

Fig. 9. (a) The CV curves of the HSC collected in diverse potential ranges at 30 mV s^{-1}, (b) The CV profiles of the HSC at different rates, (c) The GCD curves of the HSC at various current densities, (d) The specific capacitances of devices at different current densities calculated from GCD, (e) The Ragone plot of devices, (f) The comparison of Nyquist plots after and before cycling test for devices, and (g) The capacitance retention of the HSC at 5 A g^{-1} during 10,000 cycles with corresponding periodic GCD profiles.

were further calculated. The Ragone diagram is shown in Fig. 9 (e). The results indicate that energy density of CoCe/g-C_3N_4//AC HSC device maintained a higher energy density at different power densities. Specifically, the device retains energy capacities of 37.4, 29.0, 28.5, 25.0, 20.5, and 15.5 Wh kg^{-1} when operated under power densities of 749.9, 1499.9, 2249.8, 3749.9, 7500.4, and 15,008.5 W kg^{-1}, respectively. Such a high energy density exhibited by HSC device matched with the lithium-ion batteries, underscoring their potential in commercial

applications. To assess the stability and efficiency of the device, HSC was evaluated through 10,000 charge-discharge cycles conducted at a current density of 5 A g^{-1}. A comparative analysis of its electrochemical impedance was also performed before and after the cycling process as shown in Fig. 9 (f). Upon completion of the cycling process, there is a noticeable increase in R_s of the device, potentially attributed to variations in electrolyte concentration over prolonged cycling periods. Simultaneously, changes observed in R_{ct} and W_s are minimal (Table S1 for specific results), suggesting that the electrode material exhibits superior cyclic stability and outstanding ion conduction efficiency.

The exceptional electrochemical performance may be due to surface cations in Co_3O_4 (Co^{2+} and Co^{3+}), which could assist as the electronic donor/acceptor reduction sites for fast electrochemical activity. Therefore, based on this assumption, accumulating the surface exposed cations site quantity might be a possible process to further improve the electrochemical activity (Edri et al., 2017). In addition, cycle stability is also a key factor in practical applications. Fig. 9 (g) illustrates cycling stability and capacity retention across different cycling stages. Notice that during the initial 200 cycles, there was a marginal increase in capacity retention, which can be ascribed to electrode material activation process (Chen et al., 2016), after which the capacitance was stable, maintaining up to 10,000 and showed ~100% of retention rate, which indicates the fabricated HSC device has an outstanding cycling stability. As a result, enhanced electrochemical activity of the prepared electrode can be attributed to the surface oxygens permitting quick dispersion and reaction (owing to its rich Ce^{4+}/Ce^{3+}or Co^{2+} and Co^{3+}), and g-C_3N_4 in the composite could progress the charge transport between the electrode and the electrolyte as well as its higher working window potential. Hence, the fabricated HSC device shows outstanding electrochemical performance and has great potential in practical supercapacitors as well as energy storage device applications.

4. Conclusions

The CoCe/g-C_3N_4 ternary heterostructured electrodes were prepared following a simple hydrothermal technique for developing hybrid supercapacitors. The interaction between g-C_3N_4 and CoCe materials can deliver a decent connection for ion transmission and extra active sites during electrochemical reactions due to 2D lamellar g-C_3N_4 structure. Especially, CoCe/g-C_3N_4 electrode showed an ultra-high specific capacitance of 1088.3 F g^{-1} at a current density of 1 A g^{-1}, which is considerably higher than the pristine g-C_3N_4 (196.5 F g^{-1}) and CoCe (215.4 F g^{-1}) electrodes. Furthermore, fabricated HSC device has an adequate energy density of 37.4 Wh kg^{-1} at a power density of 749.9 W kg^{-1}. The improvement in electrochemical performance is attributed to 3D flower-like structure, higher electrochemical active sites, enhanced charge moving at the interface of electrode/electrolyte, higher specific surface area, ample reaction active sites, and good electrical conductivity. This study suggests a simple method and architectural strategy to achieve an extraordinary performance of HSC and other related energy storage applications. Furthermore, the distinctive electrochemical properties of CoCe/g-C_3N_4 ternary composite demonstrate its potential for applications in the development of high-performance batteries, electrocatalysis, and energy-related devices.

CRediT authorship contribution statement

Mule Vijayalakshmi: Writing – original draft, Investigation, Conceptualization. **Rui Wang:** Investigation. **Won Young Jang:** Writing – review & editing. **Raghava Reddy Kakarla:** Writing – review & editing, Methodology. **Ch Venkata Reddy:** Writing – review & editing, Supervision, Formal analysis. **Fernando Alonso-Marroquin:** Data curation, Resources. **P.M. Anjana:** Formal analysis, Methodology. **Bai Cheolho:** Funding acquisition, Formal analysis. **Jaesool Shim:** Writing – review & editing, Supervision, Funding acquisition. **Tejraj M. Aminabhavi:** Writing – review & editing, Supervision.

Declaration of competing interest

The authors declare that they have no known competing financial interests or personal relationships that could have appeared to influence the work reported in this paper.

Acknowledgments

This work was supported by the National Research Foundation (NRF) of Korea (RS-2023-00280665), Republic of Korea.

Appendix A. Supplementary data

Supplementary data to this article can be found online at https://doi.org/10.1016/j.jenvman.2024.122996.

Data availability

Data will be made available on request.

References

Ali, A.A., Nazeer, A.A., Madkour, M., Bumajdad, A., Al Sagheer, F., 2018. Novel supercapacitor electrodes based semiconductor nanoheterostructure of CdS/rGO/CeO_2 as efficient candidates. Arab. J. Chem. 11, 692–699.

Bai, L., Huang, H., Yu, S., Zhang, D., Huang, H., Zhang, Y., 2022. Role of transition metal oxides in g-C_3N_4-based heterojunctions for photocatalysis and supercapacitors. J. Energy Chem. 64, 214–235.

Bao, J., Zhang, X., Fan, B., Zhang, J., Zhou, M., Yang, W., Hu, X., Wang, H., Pan, B., Xie, Y., 2015. Ultrathin spinel-structured nanosheets rich in oxygen deficiencies for enhanced electrocatalytic water oxidation. Angew. Chem. Int. Ed. 54, 7399–7404.

Bhatt, K.P., Patel, S., Upadhyay, D.S., Patel, R.N., 2024. Production of hydrogen-rich fuel gas from waste plastics using continuous plasma pyrolysis reactor. J. Environ. Manag. 356, 120446.

Brezesinski, T., Wang, J., Tolbert, S.H., Dunn, B., 2010. Ordered mesoporous α-MoO_3 with iso-oriented nanocrystalline walls for thin-film pseudocapacitors. Nat. Mater. 9, 146–151.

Chatterjee, D.P., Nandi, A.K., 2021. A review on the recent advances in hybrid supercapacitors. J. Mater. Chem. A 9, 15880–15918.

Chau, J.H.F., Lai, C.W., Leo, B.F., Juan, J.C., Lee, K.M., Qian, X., Badruddin, I.A., Zai, J., 2024. Direct Z-scheme $Cu_2O/WO_3/TiO_2$ nanocomposite as a potential supercapacitor electrode and an effective visible-light-driven photocatalyst. J. Environ. Manag. 363, 121332.

Chen, H., Jiang, G., Yu, W., Liu, D., Liu, Y., Li, L., Huang, Q., Tong, Z., 2016. Electrospun carbon nanofibers coated with urchin-like $ZnCo_2O_4$ nanosheets as a flexible electrode material. J. Mater. Chem. A 4, 5958–5964.

Cho, E.-C., Chang-Jian, C.-W., Huang, J.-H., Chou, J.-A., Syu, W.-L., Chen, Y.-L., Lee, K.-C., Hsiao, Y.-S., 2020. Phase and morphology control in the synthesis of Co_3O_4 nanosphere/α-$Co(OH)_2$ nanosheet hybrids for application in supercapacitors. J. Taiwan Inst. Chem. Eng. 110, 163–172.

Du, L., Gao, B., Xu, S., Xu, Q., 2023. Strong ferromagnetism of g-C_3N_4 achieved by atomic manipulation. Nat. Commun. 14, 2278.

Edri, E., Cooper, J.K., Sharp, I.D., Guldi, D.M., Frei, H., 2017. Ultrafast charge transfer between light absorber and Co_3O_4 water oxidation catalyst across molecular wires embedded in silica membrane. J. Am. Chem. Soc. 139, 5458–5466.

Fu, Z., Zhang, W., Qin, D., Han, S., Dong, Z., 2024. Energy band and interface engineering of ternary TNAs/g-C_3N_4/NCQDs photoanode with enhanced optical absorption and charge transfer for efficient photoelectrochemical water oxidation. Carbon 219, 118780.

Gao, Z., Song, N., Li, X., 2015. Microstructural design of hybrid CoO@NiO and graphene nano-architectures for flexible high performance supercapacitors. J. Mater. Chem. A 3, 14833–14844.

Hadji, F., Omari, M., Mebarki, M., Gabouze, N., Layadi, A., 2023. Zinc doping effect on the structural and electrochemical properties of $LaCoO_3$ perovskite as a material for hybrid supercapacitor electrodes. J. Alloys Compd. 942, 169047.

Huang, J., Sheng, H., Ross, R.D., Han, J., Wang, X., Song, B., Jin, S., 2021a. Modifying redox properties and local bonding of Co_3O_4 by CeO_2 enhances oxygen evolution catalysis in acid. Nat. Commun. 12, 3036.

Huang, Z.-F., Xi, S., Song, J., Dou, S., Li, X., Du, Y., Diao, C., Xu, Z.J., Wang, X., 2021b. Tuning of lattice oxygen reactivity and scaling relation to construct better oxygen evolution electrocatalyst. Nat. Commun. 12, 3992.

Jang, W.Y., Reddy, C.V., Wang, R., Choi, J., Son, J., Kakarla, R.R., Aminabhavi, T.M., Shim, J., 2023. Synthesis of 1D/2D VO_2 (B) nanowire/g-C_3N_4 hybrid architectures as cathode materials for high-performance Li-ion batteries. Chem. Eng. J. 476, 146786.

Ji, F., Gou, S., Tang, J., Xu, Y., Eldin, S.M., Mai, W., Li, J., Liu, B.-T., 2023. High-performance Zn-ion hybrid supercapacitor enabled by a lightweight polyimide-based anode. Chem. Eng. J. 474, 145786.

Kandula, S., Shrestha, K.R., Rajeshkhanna, G., Kim, N.H., Lee, J.H., 2019. Kirkendall growth and ostwald ripening induced hierarchical morphology of Ni–Co LDH/

MMoSx (M = Co, Ni, and Zn) heteronanostructures as advanced electrode materials for asymmetric solid-state supercapacitors. ACS Appl. Mater. Interfaces 11, 11555–11567.
Kang, S., Zhang, Z., He, M., Fang, Z., Sun, D., Zheng, L., Chang, X., Cui, L., 2022. Harmonious K–I–O co-modification of g-C_3N_4 for improved charge separation and photocatalysis. Inorg. Chem. Front. 9, 950–958.
Kim, K.-W., Park, B., Kim, J., Seok, H., Kim, T., Jo, C., Kim, J.K., 2023. Block copolymer-directed facile synthesis of N-doped mesoporous graphitic carbon for reliable, high-performance Zn ion hybrid supercapacitor. ACS Appl. Mater. Interfaces 15, 57905–57912.
Kundu, R., Kunnoth, B., Pilli, S., Polisetty, V.R., Tyagi, R.D., 2023. Biochar symbiosis in anaerobic digestion to enhance biogas production: a comprehensive review. J. Environ. Manag. 344, 118743.
Li, L., Zhang, Y., Shi, F., Zhang, Y., Zhang, J., Gu, C., Wang, X., Tu, J., 2014. Spinel manganese–nickel–cobalt ternary oxide nanowire array for high-performance electrochemical capacitor applications. ACS Appl. Mater. Interfaces 6, 18040–18047.
Li, B., Ge, X., Goh, F.W.T., Hor, T.S.A., Geng, D., Du, G., Liu, Z., Zhang, J., Liu, X., Zong, Y., 2015. Co_3O_4 nanoparticles decorated carbon nanofiber mat as binder-free air-cathode for high performance rechargeable zinc-air batteries. Nanoscale 7, 1830–1838.
Li, Z., Zhao, D., Xu, C., Ning, J., Zhong, Y., Zhang, Z., Wang, Y., Hu, Y., 2018. Reduced $CoNi_2S_4$ nanosheets with enhanced conductivity for high-performance supercapacitors. Electrochim. Acta 278, 33–41.
Li, J., Kang, Y., Lei, Z., Liu, P., 2023. Well-controlled 3D flower-like CoP_3/CeO_2/C heterostructures as bifunctional oxygen electrocatalysts for rechargeable Zn-air batteries. Appl. Catal. B Environ. 321, 122029.
Lian, Q., Zhou, G., Zeng, X., Wu, C., Wei, Y., Cui, C., Wei, W., Chen, L., Li, C., 2016. Carbon coated SnS/SnO_2 heterostructures wrapping on CNFs as an improved-performance anode for Li-ion batteries: lithiation-induced structural optimization upon cycling. ACS Appl. Mater. Interfaces 8, 30256–30263.
Liu, Y., Wang, Z., Zhong, Y., Tade, M., Zhou, W., Shao, Z., 2017. Molecular design of mesoporous $NiCo_2O_4$ and $NiCo_2S_4$ with sub-micrometer-polyhedron architectures for efficient pseudocapacitive energy storage. Adv. Funct. Mater. 27, 1701229.
Liu, Z., Li, J., Buettner, M., Ranganathan, R.V., Uddi, M., Wang, R., 2019. Metal–support interactions in CeO_2- and SiO_2-supported cobalt catalysts: effect of support morphology, reducibility, and interfacial configuration. ACS Appl. Mater. Interfaces 11, 17035–17049.
Lu, W., Shen, J., Zhang, P., Zhong, Y., Hu, Y., Lou, X.W., 2019. Construction of CoO/Co-Cu-S hierarchical tubular heterostructures for hybrid supercapacitors. Angew. Chem. Int. Ed. 58, 15441–15447.
Lv, L.-B., Ye, T.-N., Gong, L.-H., Wang, K.-X., Su, J., Li, X.-H., Chen, J.-S., 2015. Anchoring cobalt nanocrystals through the plane of graphene: highly integrated electrocatalyst for oxygen reduction reaction. Chem. Mater. 27, 544–549.
Ma, K., Cheng, J.P., Zhang, J., Li, M., Liu, F., Zhang, X., 2016. Dependence of Co/Fe ratios in Co-Fe layered double hydroxides on the structure and capacitive properties. Electrochim. Acta 198, 231–240.
Maruthasalamoorthy, S., Aishwarya, K., Thenmozhi, R., Nirmala, R., Nagarajan, C., Navamathavan, R., 2023. Superior cyclic stability and electrochemical performance of La supported Bi_2S_3@g-C_3N_4//rGO heterostructure composite for asymmetric supercapacitor devices. J. Alloys Compd. 967, 171696.
Qi, J., Zhao, K., Li, G., Gao, Y., Zhao, H., Yu, R., Tang, Z., 2014. Multi-shelled CeO_2 hollow microspheres as superior photocatalysts for water oxidation. Nanoscale 6, 4072–4077.
Qiao, F., Liu, W., Wang, S., Lin, F., Chen, Y., Yuan, M., Weng, Z., Wang, S., Zheng, J., Zhao, Y., 2021. Hierarchical Co_3S_4/CoS/MoS_2 leaf-like nanoflakes array derived from Co-ZIF-L as an advanced anode for flexible supercapacitor. J. Alloys Compd. 870, 159393.
Rabani, I., Karuppasamy, K., Vikraman, D., ul haq, Z., Kim, H.-S., Seo, Y.-S., 2021. Hierarchical structured nano-polyhedrons of CeO_2@ZIF-8 composite for high performance supercapacitor applications. J. Alloys Compd. 875, 160074.
Rabbani, S.S., Mustafa, H., Zafar, A., Javaid, S., Bakar, M.A., Nisar, A., Liu, Y., Karim, S., Sun, H., Hussain, S., Zafar, Z., Faiz, Y., Faiz, F., Yu, Y., Ahmad, M., 2023. Nickel foam supported hierarchical $NiCo_2S_4$@NiFe LDH heterostructures as highly efficient electrode for long cycling stability supercapacitor. Electrochim. Acta 446, 142098.
Reddy, N.R., Reddy, P.M., Mandal, T.K., Reddy, K.R., Shetti, N.P., Saleh, T.A., Joo, S.W., Aminabhavi, T.M., 2021. Synthesis of novel Co_3O_4 nanocubes-NiO octahedral hybrids for electrochemical energy storage supercapacitors. J. Environ. Manag. 298, 113484.
Reddy, C.V., Reddy, I.N., Koutavarapu, R., Reddy, K.R., Saleh, T.A., Aminabhavi, T.M., Shim, J., 2022. Novel edge-capped ZrO_2 nanoparticles onto V_2O_5 nanowires for efficient photosensitized reduction of chromium (Cr (VI)), photoelectrochemical solar water splitting, and electrochemical energy storage applications. Chem. Eng. J. 430, 132988.
Riyajuddin, S., Azmi, K., Pahuja, M., Kumar, S., Maruyama, T., Bera, C., Ghosh, K., 2021. Super-hydrophilic hierarchical Ni-Foam-Graphene-Carbon nanotubes-Ni_2P–CuP_2 nano-architecture as efficient electrocatalyst for overall water splitting. ACS Nano 15, 5586–5599.
Roy, A., Inta, H.R., Ghosh, S., Koppisetti, H.V.S.R.M., Mondal, A., Verma, B.R., Bag, S., Mahalingam, V., 2024. Electrochemical surface reconstruction of nickel cobalt pyrophosphate to Ni/Co-hydroxide-(oxy)hydroxide: an efficient and highly durable battery-type supercapacitor electrode material. J. Mater. Chem. A 12, 4086–4098.
Sethi, M., Shenoy, U.S., Bhat, D.K., 2020. A porous graphene–$NiFe_2O_4$ nanocomposite with high electrochemical performance and high cycling stability for energy storage applications. Nanoscale Adv. 2, 4229–4241.
Shao, Y., El-Kady, M.F., Sun, J., Li, Y., Zhang, Q., Zhu, M., Wang, H., Dunn, B., Kaner, R. B., 2018. Design and mechanisms of asymmetric supercapacitors. Chem. Rev. 118, 9233–9280.
Shin, M., Sharma, K.P., Kim, K., Awasthi, G.P., Yu, C., 2023. The morphology and phase conversion of MnO_2 in g-CN@MnO_2 composite with supercapacitor applications. J. Phys. Chem. Solid. 177, 111310.
Song, K., Li, W., Xin, J., Zheng, Y., Chen, X., Yang, R., Lv, W., Li, Q., 2021. Hierarchical porous heterostructured $Co(OH)_2/CoSe_2$ nanoarray: a controllable design electrode for advanced asymmetrical supercapacitors. Chem. Eng. J. 419, 129435.
Sun, X., Liu, X., Wang, J., Jiang, X., Liu, R., Li, A., Li, W., 2020. Nanobundles structural Co-HKUST on the foamed nickel with a high supercapacitor performance. SN Appl. Sci. 2, 414.
Tareen, A.K., Khan, K., Iqbal, M., Zhang, Y., Long, J., Nazeer, F., Mahmood, A., Mahmood, N., Shi, Z., Ma, C., Huan, W., Khan, M.F., Yin, J., Li, C., Zhang, H., 2022. Recent advances in novel graphene: new horizons in renewable energy storage technologies. J. Mater. Chem. C 10, 11472–11531.
Tian, Y., Zhou, M., Meng, X., Miao, Y., Zhang, D., 2017. Needle-like CoMoO with multi-modal porosity for pseudocapacitors. Mater. Chem. Phys. 198, 258–265.
Tuna, O., Mert, H.H., Mert, M.S., Simsek, E.B., 2024. Tubular graphitic carbon nitride-anchored on porous diatomite for enhanced solar energy efficiency in photocatalytic remediation and energy storage performance. J. Environ. Manag. 366, 121891.
Wang, J., Polleux, J., Lim, J., Dunn, B., 2007. Pseudocapacitive contributions to electrochemical energy storage in TiO_2 (anatase) nanoparticles. J. Phys. Chem. C 111, 14925–14931.
Wang, J., Shi, X., Chen, L., Li, H., Mao, M., Zhang, G., Yi, H., Fu, M., Ye, D., Wu, J., 2021a. Enhanced performance of low Pt loading amount on Pt-CeO_2 catalysts prepared by adsorption method for catalytic ozonation of toluene. Appl. Catal. Gen. 625, 118342.
Wang, B., Gao, R., Zhang, D., Zeng, Y., Zhang, F., Yan, X., Li, Y., Chen, L., 2021b. Ceria-promoted Co@NC catalyst for biofuel upgrade: synergy between ceria and cobalt species. J. Mater. Chem. A 9, 8541–8553.
Wang, R., Young Jang, W., Zhang, W., Venkata Reddy, C., Kakarla, R.R., Li, C., Gupta, V. K., Shim, J., Aminabhavi, T.M., 2023a. Emerging two-dimensional (2D) MXene-based nanostructured materials: synthesis strategies, properties, and applications as efficient pseudo-supercapacitors. Chem. Eng. J. 472, 144913.
Wang, H., Zhang, Q., Sun, F., Qi, J., Zhang, D., Sun, H., Li, Z., Wang, Q., Wang, B., 2023b. Construction of Co_3O_4/CeO_2 heterostructure nanoflowers facilitates deployment of oxygen defects to enhance the oxygen evolution kinetics. J. Alloys Compd. 933, 167700.
Xia, J., Zhao, H., Huang, B., Xu, L., Luo, M., Wang, J., Luo, F., Du, Y., Yan, C.-H., 2020. Efficient optimization of electron/oxygen pathway by constructing ceria/hydroxide interface for highly active oxygen evolution reaction. Adv. Funct. Mater. 30, 1908367.
Xiao, Z., Do, H., Yusuf, A., Jia, H., Ma, H., Jiang, S., Li, J., Sun, Y., Wang, C., Ren, Y., Chen, G.Z., He, J., 2024. Facile synthesis of multi-layer $Co(OH)_2/CeO_2$-g-C_3N_4 ternary synergistic heterostructure for efficient photocatalytic oxidation of NO under visible light. J. Hazard Mater. 462, 132744.
Xie, H., Mao, L., Mao, J., 2021. Structural evolution of $Ce[Fe(CN)_6]$ and derived porous Fe-CeO_2 with high performance for supercapacitor. Chem. Eng. J. 421, 127826.
Yang, K., Hu, Y., Li, L., Cui, L., He, L., Wang, S., Zhao, J., Song, Y.-F., 2020. First high-nuclearity mixed-valence polyoxometalate with hierarchical interconnected Zn^{2+} migration channels as an advanced cathode material in aqueous zinc-ion battery. Nano Energy 74, 104851.
Yi, S., Lai, P., Ma, G., Pan, J., Chen, Z., Qin, Y., Jiang, X., 2023. Green and facile synthesis of nanostructured Co_3O_4/CeO_2 catalysts via a glucose-urea method for NO oxidation. Appl. Surf. Sci. 626, 157180.
Young Jang, W., Venkata Reddy, C., Daouli, A., Kakarla, R.R., Bandaru, N., Shim, J., Badawi, M., Aminabhavi, T.M., 2023. Novel 2D sulfur-doped V_2O_5 flakes and their applications in photoelectrochemical water oxidation and high-performance energy storage supercapacitors. Chem. Eng. J. 461, 141935.
Zeng, W., Zhang, G., Wu, X., Zhang, K., Zhang, H., Hou, S., Li, C., Wang, T., Duan, H., 2015. Construction of hierarchical CoS nanowire@$NiCo_2S_4$ nanosheet arrays via one-step ion exchange for high-performance supercapacitors. J. Mater. Chem. A 3, 24033–24040.
Zhang, Y., Pan, A., Wang, Y., Cao, X., Zhou, Z., Zhu, T., Liang, S., Cao, G., 2017a. Self-templated synthesis of N-doped $CoSe_2$/C double-shelled dodecahedra for high-performance supercapacitors. Energy Storage Mater. 8, 28–34.
Zhang, S., Huang, Z.-Q., Ma, Y., Gao, W., Li, J., Cao, F., Li, L., Chang, C.-R., Qu, Y., 2017b. Solid frustrated-Lewis-pair catalysts constructed by regulations on surface defects of porous nanorods of CeO_2. Nat. Commun. 8, 15266.
Zhang, S., Gu, P., Ma, R., Luo, C., Wen, T., Zhao, G., Cheng, W., Wang, X., 2019. Recent developments in fabrication and structure regulation of visible-light-driven g-C_3N_4-based photocatalysts towards water purification: a critical review. Catal. Today 335, 65–77.
Zhang, X., Wang, Y., Qiao, Z., Yu, X., Ruan, D., 2022. D. Regeneration and usage of commercial activated carbon from the waste electrodes for the application of supercapacitors. J. Environ. Manag. 322, 116083.
Zhang, Y., Huang, W., Zhao, K., Zhang, M., Guo, H., Liu, J., 2023. Solvothermal synthesis of CoCeSx quantum dots based on Bi-pyrene-terminated molecular wires modified porous graphene for high performance supercapacitors. J. Alloys Compd. 932, 167614.
Zheng, Y., Zhou, T., Zhang, C., Mao, J., Liu, H., Guo, Z., 2016. Boosted charge transfer in SnS/SnO_2 heterostructures: toward high rate capability for sodium-ion batteries. Angew. Chem. Int. Ed. 55, 3408–3413.
Zhong, J., Zeng, Y., Zhang, M., Feng, W., Xiao, D., Wu, J., Chen, P., Fu, M., Ye, D., 2020. Toluene oxidation process and proper mechanism over Co_3O_4 nanotubes:

Investigation through in-situ DRIFTS combined with PTR-TOF-MS and quasi in-situ XPS. Chem. Eng. J. 397, 125375.